

RESEARCH ARTICLE

10.1029/2018JA026417

Key Points:

- The electron distribution and whistler wave characteristics are significantly different in the core and draping regions of the FTEs
- The close correlation between the pancake distribution and compression of the localized magnetic field is observed in the trailing part
- The whistler waves associated with the FTEs are categorized into the lower and upper bands according to the frequency range

Correspondence to:

R. Wang and Q. Lu,
rswan@ustc.edu.cn;
qmlu@ustc.edu.cn

Citation:

Wang, S., Wang, R., Yao, S. T., Lu, Q., Russell, C. T., & Wang, S. (2019). Anisotropic electron distributions and whistler waves in a series of the flux transfer events at the magnetopause. *Journal of Geophysical Research: Space Physics*, 124, 1753–1769. <https://doi.org/10.1029/2018JA026417>






Received 19 DEC 2018

Accepted 28 FEB 2019

Accepted article online 7 MAR 2019

Published online 25 MAR 2019

Anisotropic Electron Distributions and Whistler Waves in a Series of the Flux Transfer Events at the Magnetopause

Shimou Wang^{1,2} , Rongsheng Wang^{1,2} , S. T. Yao³ , Quanming Lu^{1,2} , C. T. Russell⁴ , and Shui Wang^{1,2}

¹CAS Key Laboratory of Geospace Environment, Department of Geophysics and Planetary Science, University of Science and Technology of China, Hefei, China, ²CAS Center for Excellence in Comparative Planetology, Hefei, China, ³Shandong Provincial Key Laboratory of Optical Astronomy and Solar-Terrestrial Environment, Institute of Space Sciences, Shandong University, Weihai, China, ⁴Department of Earth, Planetary, and Space Sciences, University of California, Los Angeles, CA, USA

Abstract With the measurements of the Magnetospheric Multiscale mission at the magnetopause, we investigated the electron distribution and the whistler waves associated with a series of six ion-scale flux transfer events (FTEs). Based on the magnetic field signature, each FTE can be divided into the core region and the draping region. In the draping regions of the most FTEs, the low-energy electrons displayed a bidirectional field-aligned distribution. The medium-energy electrons showed a field-aligned or beam distribution in the leading part, while a pancake distribution was presented for the electrons in the trailing part of the draping region, which has never been reported previously. The close correlation between the pancake distribution and the compression of the localized magnetic field suggests that the pancake distribution may be due to the betatron acceleration. The whistler waves associated with the FTEs were observed and categorized into the lower and upper bands according to the frequency range. The lower band whistler waves propagated in variable directions and therefore could be generated locally. The trailing part of the draping region with the electron pancake distribution was considered to be one possible source region. On the contrary, the upper band whistler waves were all found in the core region and propagated antiparallel to the magnetic field and therefore originated from the same source region. The observations confirmed that the FTEs are important channels for the mass and wave transport between the magnetosheath and the inner magnetosphere, and the electron dynamics can be modified during the FTE evolution.

1. Introduction

Flux transfer events (FTEs) representing the helical magnetic structures are frequently observed at the magnetopause. The typical signatures of the FTEs are a bipolar variation of the magnetic field component in the normal direction of the magnetopause and a strong core field along their axes (Russell & Elphic, 1978). The FTEs at the magnetopause are widely considered to be related to magnetic reconnection (Hasegawa et al., 2010; Lee & Fu, 1985; Oieroset et al., 2011; Russell & Elphic, 1978; Scholer, 1988; Southwood et al., 1988; Tan et al., 2011), which modifies the topological structure of the magnetic field and transfers mass and energy from solar wind into the Earth's magnetosphere. The properties of FTEs have been extensively studied since the concept was first proposed (Fear et al., 2008; Kawano & Russell, 1997; Owen et al., 2008; Paschmann et al., 1982; Saunders et al., 1984; Zhang et al., 2012). Previous observations found that the plasma density was lower inside the FTEs as compared with that at the boundary (Oieroset et al., 2011). Varsani et al. (2014) used the Cluster data to reconstruct the high time resolution pitch angle distributions of electrons and ions and suggested that the FTE consisted of multiple different plasma layers.

The Magnetospheric Multiscale (MMS) mission launched by the National Aeronautics and Space Administration on 12 March 2015 (Burch et al., 2016) has a huge improvement in time resolution for plasma and fields measurements and will improve our understanding of the FTEs, especially the electron dynamics inside the FTEs. A series of five ion-scale flux ropes have been identified near the reconnection ion diffusion region at the magnetopause, and they were propagating obliquely to the guide field (Teh et al., 2017) rather than perpendicular to it. A few filamentary currents and the deviation of the ion-frozen-in condition were found inside ion-scale flux ropes (Eastwood et al., 2016; Teh et al., 2017;

Wang et al., 2017). The plasma distribution inside a FTE has been investigated by the MMS measurements (Hwang et al., 2016). A kind of D-shaped ion distributions and the isotropic electron distribution have been observed inside this FTE.

In this paper, we investigated a series of six FTEs observed in the southward outflow at the magnetopause on 10 January 2016. The first two FTEs were found to be very close to the electron diffusion region, while the other four FTEs were far away from the region. The electron distribution was complex in these FTEs. The whistler mode waves can be observed around these FTEs.

2. Database and Observation

The MMS mission consists of four spacecraft forming a typical tetrahedron with adjustable interspacecraft separation down to 10 km. In the interesting regions (e.g., reconnection region and plasma sheet), the burst data are collected (Burch et al., 2016). In this paper, the magnetic field data with a sample rate of 128/s from fluxgate magnetometer instrument (Russell et al., 2016) are used. The electric field data are measured with the spin-plane double probe and the axial double probe instrument sampled at 8,192/s (Ergun et al., 2016; Lindqvist et al., 2016). Electrons and ions distributions are obtained from the fast plasma investigation with an unprecedented time resolution: 30 ms for electrons and 150 ms for ions (Pollock et al., 2016). The magnetic field data with a sample rate of 8,192/s from the search-coil magnetometer are used for wave analysis (Le Contel et al., 2016).

2.1. Overview of the Event

On 10 January 2016, MMS passed through the magnetopause from magnetosheath to magnetosphere at ~09:00 UT. At that time, MMS was located at $[9.0, -2.6, -0.9] R_E$ in the Geocentric Solar Ecliptic (GSE) coordinate system, approximately at the subsolar point; hence, the GSE coordinate system is appropriate in the event. During this crossing, the ion flows were strong and southward (up to the local Alfvén speed), that is, the reconnection was occurring within the current sheet. Figure 1 presents an overview of the FTEs in the GSE coordinate system. Since the separation of the four satellites was only about 40 km, the measurements at them were similar and thus only the data from MMS1 was displayed. The event was observed between 08:58:45 and 09:01:30 UT. Figure 1a presents the omnidirectional electron energy spectrum. Figure 1b shows three components of magnetic field (B_x in blue, B_y in green, and B_z in red) and the magnetic field intensity (in black). Figure 1c shows plasma number density. Figures 1d and 1e show ion flows and electron flows, respectively. Figures 1f and 1g present ion and electron temperatures including parallel (blue) and perpendicular (red) temperatures. Figure 1h shows the parallel electric field (green curve) and its error in pink shadow. In this interval, the spacecraft was mainly located in the magnetopause boundary layer, since the low-energy magnetosheath populations (~100 eV) and the high-energy magnetosphere populations (>1 keV) were observed simultaneously (Figure 1a), and additionally, the plasma density was between 5 and 40 cm^{-3} (Figure 1c). The southward ion flows were continuously observed and the speed, sometimes, reached 400 km/s, $\sim 0.8 V_A$ where V_A is the Alfvén speed derived from $B = 70$ nT and $N = 10$ cm^{-3} . It implies that the reconnection X-line was north of the spacecraft. In the whole interval, we identified six FTEs characterized by a bipolar signature of B_x and an enhancement of B_y and $|\mathbf{B}|$ (Figure 1b) near the reversal points of B_x . The FTEs were in pairs in this event, and thereby the intervals including the FTEs were labeled as B, C, and D in time sequence. Namely, each short interval (B, C, and D) consists of two FTEs. Before the FTEs, there existed a period of 08:58:55–08:59:08 UT (labeled as A) when the super-Alfvén electron flows were detected.

In the interval of A, the high-speed electron flows exceeding 1,500 km/s were observed (Figure 1e) and were mainly streaming southward. At the same time, the ion flow speed declined from ~400 to ~150 km/s in the $-z$ direction. Comparing the electron flows V_{ez} with ion flows V_{iz} , we found that the electron bulk flows were much stronger than the ion flows (Figures 1d and 1e). Inside the high-speed electron flows, both the ions and electrons were heated. The ions were heated in both the parallel and perpendicular directions, and their perpendicular temperature was mostly higher than the parallel temperature (Figure 1f) in the region. In contrast, although the electrons were also heated in both directions, the parallel temperature was significantly higher than the perpendicular temperature (Figure 1g). Inside the electron flows, the parallel electric field

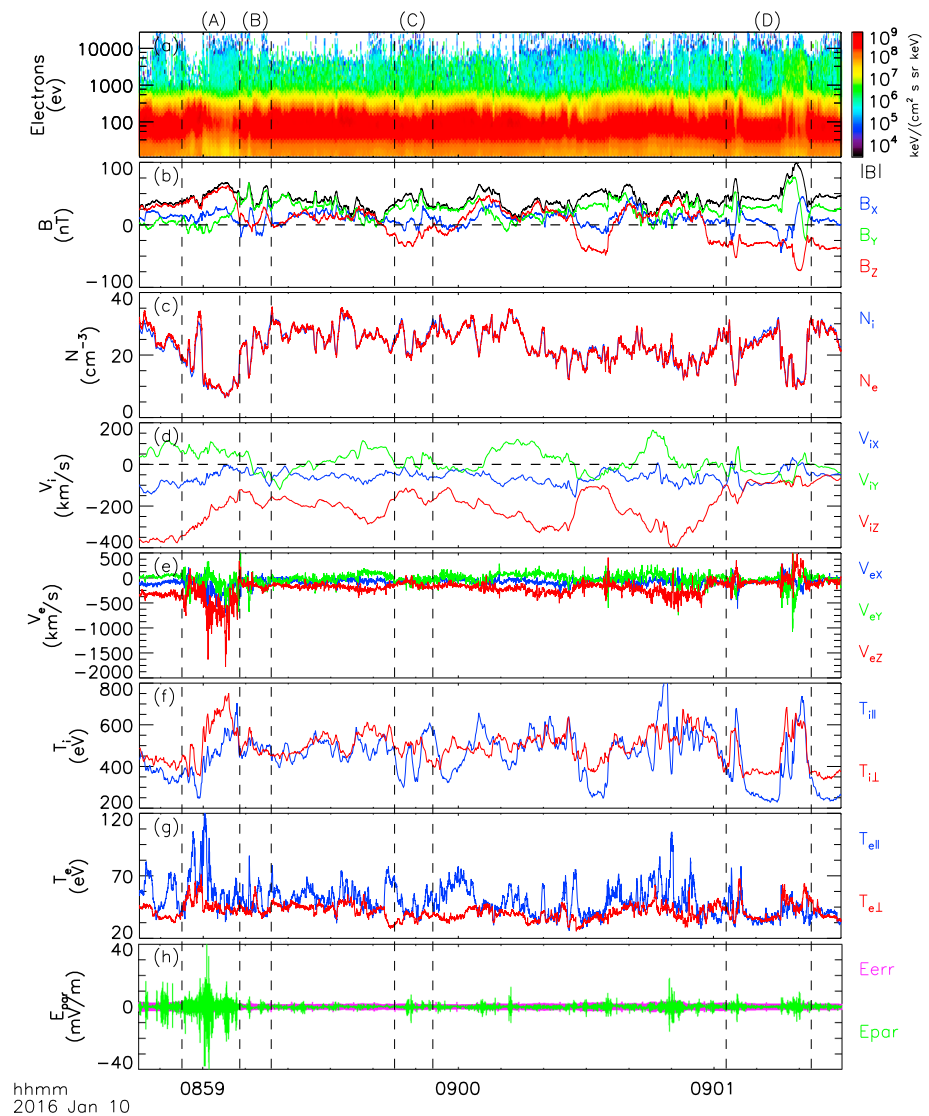


Figure 1. An overview of the whole events. (a) Omnidirectional electron energy spectrum, (b) three components and magnitude of magnetic field, (c) density, (d) ion flows, (e) electron flows, (f) ion temperature, (g) electron temperature, and (h) parallel electric field. Data of MMS1 are shown.

was intense and its amplitude exceeded 40 mV/m (Figure 1h). Therefore, we conclude that the spacecraft was close to the electron diffusion region and within the ion diffusion region in this initial period.

The ion diffusion region labeled “A” and the adjacent period “B” are zoomed-in in Figure 2. Figures 2a and 2b show three components of the magnetic field and the electron bulk flow. The x and y components of the measured electric field in blue, $-(\mathbf{V}_i \times \mathbf{B})$ in green, and $-(\mathbf{V}_e \times \mathbf{B})$ in red are shown in Figures 2c and 2d, respectively. Figure 2e shows $\mathbf{J} \cdot (\mathbf{E} + \mathbf{V}_e \times \mathbf{B})$ and its parallel and perpendicular components. It is clear from Figures 2c and 2d that $-(\mathbf{V}_i \times \mathbf{B})$ was largely deviated from \mathbf{E} and $-(\mathbf{V}_e \times \mathbf{B})$ during 08:58:56–08:59:10 UT, whereas \mathbf{E} and $-(\mathbf{V}_e \times \mathbf{B})$ matched very well. It means that the electrons were roughly frozen in the magnetic field while the ions were no longer frozen in the magnetic field. This observation further supports the conclusion that the ion diffusion region was encountered by the spacecraft during 08:58:55–08:59:10 UT. The energy dissipation in the electron frame is shown in Figure 2e. The values of $\mathbf{J} \cdot (\mathbf{E} + \mathbf{V}_e \times \mathbf{B})$ varied largely inside the ion diffusion region and were mainly negative from ~08:58:56 to ~08:58:59 UT and from ~08:59:05 to ~08:59:08 UT. Namely, the values of $\mathbf{J} \cdot (\mathbf{E} + \mathbf{V}_e \times \mathbf{B})$ were mainly negative at the two edges of the electron flows. It indicates that the magnetic energy was accumulated in these localized regions, as reported near the electron diffusion region at the magnetopause (Wang et al., 2017).

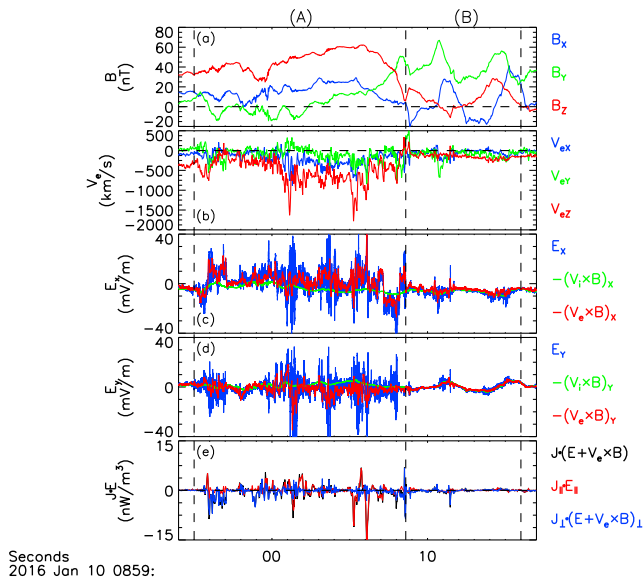


Figure 2. (a) Three components of magnetic field, (b) electron flows, (c) the electric field E_x , $-(\mathbf{V}_i \times \mathbf{B})_x$, $-(\mathbf{V}_e \times \mathbf{B})_x$, (d) the electric field E_y , $-(\mathbf{V}_i \times \mathbf{B})_y$, $-(\mathbf{V}_e \times \mathbf{B})_y$, and (e) $\mathbf{J} \cdot (\mathbf{E} + \mathbf{V}_e \times \mathbf{B})$, $\mathbf{J}_{\parallel} \cdot \mathbf{E}_{\parallel}$, $\mathbf{J}_{\perp} \cdot (\mathbf{E} + \mathbf{V}_e \times \mathbf{B})_{\perp}$.

the electron temperature, the current density, the ratio of the perpendicular and parallel currents, and the electric field in the x component (E_x , $-(\mathbf{V}_i \times \mathbf{B})_x$, and $-(\mathbf{V}_e \times \mathbf{B})_x$) are displayed from top to bottom. The current density is directly calculated from the high-resolution plasma measurements by the formula $\mathbf{J} = Nq(\mathbf{V}_i - \mathbf{V}_e)$, where N is the electron number density, q is the elementary charge, and \mathbf{V}_i and \mathbf{V}_e are the ion and electron velocity vectors.

The FTEs were observed by all four satellites of MMS in turn, so the timing method (Schwartz, 1998) was used to estimate their speeds and spatial scales. In order to obtain the accurate values, we chose the magnetic signatures of the FTEs with an evident time delay between any two of the four satellites. Eventually, the timing method was performed to the points of $B_x = 0$ for the FTE2, FTE3, and FTE5 and to the B_y peaks for the other three FTEs. The speed and the propagation direction of the six FTEs were found to be 88 km/s along $\mathbf{n1} = (-0.60, 0.06, -0.80)$ GSE for FTE1, 169 km/s along $\mathbf{n2} = (0.09, -0.29, -0.95)$ GSE for FTE2, 48 km/s along $\mathbf{n3} = (0.72, -0.28, -0.64)$ GSE for FTE3, 201 km/s along $\mathbf{n4} = (-0.58, -0.22, -0.79)$ GSE for FTE4, 119 km/s along $\mathbf{n5} = (0.04, -0.69, -0.72)$ GSE for FTE5, and 120 km/s along $\mathbf{n6} = (-0.12, -0.40, -0.91)$ GSE for FTE6. The durations of the six FTEs were ~ 2.3 , ~ 1.5 , ~ 1.8 , ~ 1.0 , ~ 1.3 , and ~ 5.2 s, respectively. Thus, the diameters of the six FTEs from FTE1 to FTE6 were ~ 202 km ($\sim 4.0d_i$), ~ 254 km ($\sim 5.0d_i$), ~ 86 km ($\sim 1.7d_i$), ~ 201 km ($\sim 3.9d_i$), ~ 155 km ($\sim 3.0d_i$), and ~ 624 km ($\sim 12.2d_i$), respectively, where the ion inertial length d_i was about 51 km according to the average density of 20 cm^{-3} . We also used the Minimal Directional Derivative and Spatial Temporal Difference methods to calculate FTEs velocity (Shi et al., 2005; Shi et al., 2006; Shi et al., 2013; Yao et al., 2016). The results (not shown here) are consistent with the timing results.

The FTEs in our event were divided into two regions, that is, draping region and core region, as done previously by Zhao et al. (2016). The interval between minimum and maximum of the magnetic field component B_x was defined as the core region, and the core region was draped by the magnetic fluxes in the draping region where B_x and $|\mathbf{B}|$ gradually faded to the ambient field. The core and draping regions were marked with the red and blue bars at the top of Figures 3–5, respectively. Thus, each core region was bounded by the leading part and trailing part of the draping region, while the spacecraft crossed the core region of a FTE.

The omnidirectional electron energy spectrum exhibits a similar feature in all of these FTEs (Figures 3b, 4b, 5b, and 5m). The fluxes of the electrons with energy less than ~ 100 eV fell in the core regions of all of the FTEs except FTE1. Although the fluxes of electrons increased in some local region of FTE1, a flux

Just after the ion diffusion region, a series of six FTEs was observed. The criteria for identifying the FTEs include a bipolar signature of the B_x component and the significant enhancement of the B_y component as well as $|\mathbf{B}|$. For the FTE1 and FTE2, they were adjacent to the ion diffusion region, especially for the FTE1, shown in Figure 3. The other four FTEs were observed in pairs also at $\sim 08:59:50$ and at $\sim 09:01:10$ UT and individually displayed in Figures 4 and 5. Since the FTE1 was encountered just near the ion diffusion region, it should be newly formed during the reconnection, that is, so-called vivo or active FTE (e.g., Pu et al., 2013). After the FTE1, the reconnection was ongoing and the reconnection site should be moving northward, because the southward ion flows were continuously observed and the ion diffusion region was no longer observed. Thus, the other FTEs 2–6 should be encountered away from the reconnection diffusion region. In other words, these flux ropes should be full grown when they were encountered.

2.2. Characteristics of the Ion-Scale FTEs

Figures 3 (for FTE1 and FTE2), 4 (for FTE3 and FTE4), and 5 (for FTE5 and FTE6) show the measurements of the FTEs in the same format. In each figure, the omnidirectional ion and electron energy spectrum, the pitch angle distribution for the low-energy (0–200 eV), middle-energy (0.2–2 keV), and high-energy (2–30 keV) electrons, three components of magnetic field and the magnetic field strength, the number densities,

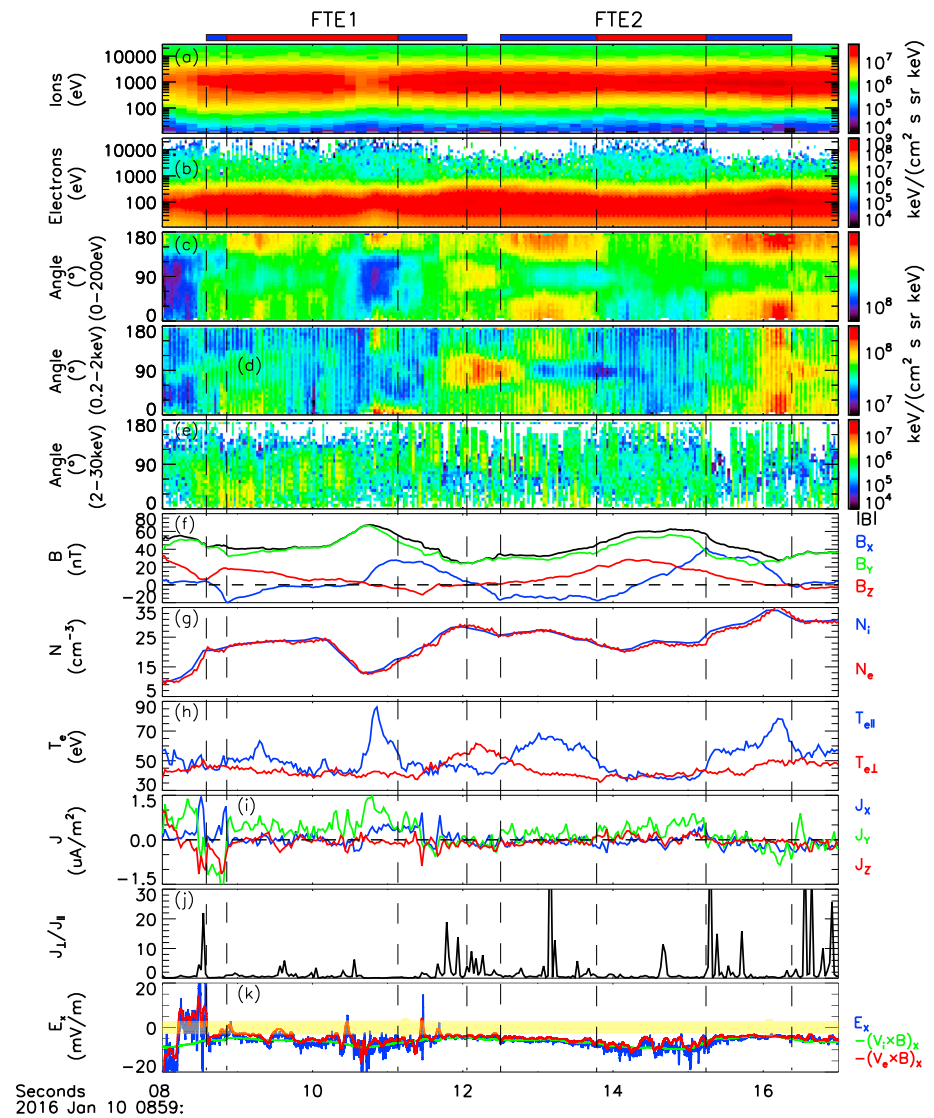


Figure 3. (a) Omnidirectional ion energy spectrum, (b) omnidirectional electron energy spectrum, (c) pitch angle spectrogram for 0 to 200 eV electrons, (d) pitch angle spectrogram for 0.2 to 2 keV electrons, (e) pitch angle spectrogram for 2 to 30 keV electrons, (f) three components and magnitude of magnetic field, (g) density, (h) electron temperature, (i) current density, (j) the ratio of $J_{\perp} / J_{\parallel}$, and (k) the electric field E_x , $-(\mathbf{v}_i \times \mathbf{B})_x$, $-(\mathbf{v}_e \times \mathbf{B})_x$, and the shadow means the errors of E_x , for the FTE1 and FTE2.

decrease still can be observed in the B_y and $|\mathbf{B}|$ peak. In contrast, the fluxes of the electrons with energy larger than 1 keV increased significantly except FTE1. The fluxes of the ions less than ~ 1 keV decreased also inside FTEs 3–6 (Figures 3a, 4a, 5a, and 5l). The decrease of the low-energy electron and ion fluxes was consistent with the plasma density dips in the core regions of these FTEs (Figures 3g, 4g, 5g, and 5r).

The electron pitch angle distributions inside the FTEs are displayed from panels (c) to (e) with different energy levels in Figures 3–5. The distributions were very complicated inside these FTEs. In the draping regions, the low-energy electron (< 200 eV) fluxes were enhanced around 0° and 180° relative to the ambient magnetic field, that is, the bidirectional field-aligned streaming (Figures 3c, 4c, and 5c) except for those of the FTE6 where the low-energy electron fluxes were enriched, sometimes, in field-aligned directions ($\sim 09:01:22.1$ UT), sometimes, in the perpendicular directions ($\sim 09:01:15.5$ and $\sim 09:01:22.7$ UT).

In the trailing parts of the draping regions of all the FTEs, the medium energy (0.2–2 keV) electron fluxes (Figures 3d, 4d, 5d, and 5o) were heightened at $\sim 90^\circ$ direction. In contrast, the medium-energy electrons

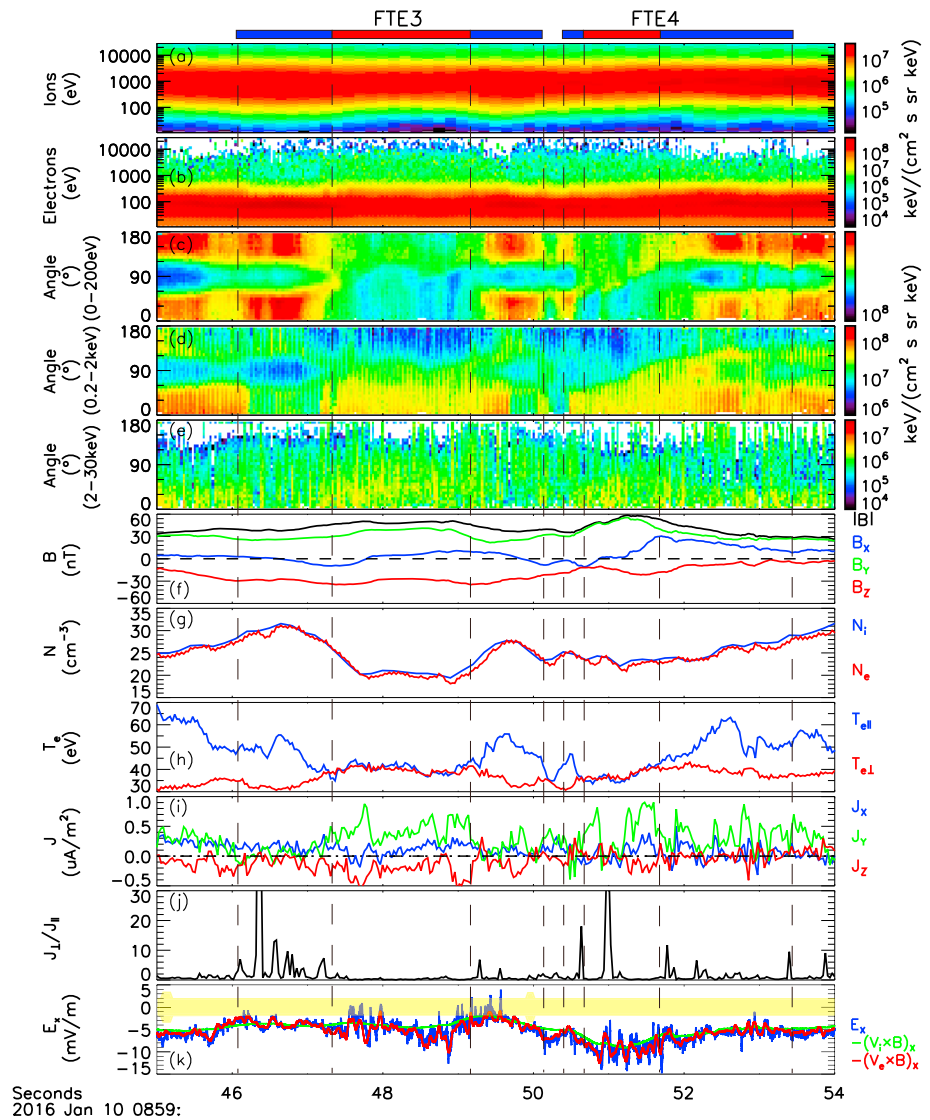


Figure 4. (a) Omnidirectional ion energy spectrum, (b) omnidirectional electron energy spectrum, (c) pitch angle spectrogram for 0 to 200 eV electrons, (d) pitch angle spectrogram for 0.2 to 2 keV electrons, (e) pitch angle spectrogram for 2 to 30 keV electrons, (f) three components and magnitude of magnetic field, (g) density, (h) electron temperature, (i) current density, (j) the ratio of J_{\perp}/J_{\parallel} , and (k) the electric field E_x , $-(\mathbf{v}_i \times \mathbf{B})_x$, $-(\mathbf{v}_e \times \mathbf{B})_x$, and the shadow means the errors of E_x , for the FTE3 and FTE4.

showed the bidirectional field-aligned distributions in the leading parts of the FTEs 2 and 3 and the beam distribution in the leading part of the FTEs 1 and 4–6. The increments of the medium-energy electron fluxes at $\sim 90^\circ$ direction in the trailing part of the draping region depended on the strength of the total magnetic field and B_x therein. For the strong magnetic field strength and the significant enhancements of B_x , the increments of the medium-energy electron fluxes were substantial, for example, FTEs 1, 2, and 4–6. While the $|\mathbf{B}|$ increment was slight in the trailing part of the FTE3, the enhancement of the medium-energy electron fluxes near 90° directions was weak also.

In the core regions of these FTEs, the low-energy electrons were mainly antiparallel streaming (Figures 3c, 4c, 5c, and 5n); the medium-energy and high-energy electrons were mainly parallel streaming (Figures 3d and 3e, 4d and 4e, 5d and 5e, and 5o and 5p), except for FTE1 and FTE2. In the core region of the FTE1, the bidirectional field-aligned distribution still can be detected as in the draping region. In the core region of the FTE2, the low-energy electron fluxes were enhanced along the $\sim 180^\circ$ direction as others, but the medium-energy fluxes were depressed in all of the directions (Figure 3d).

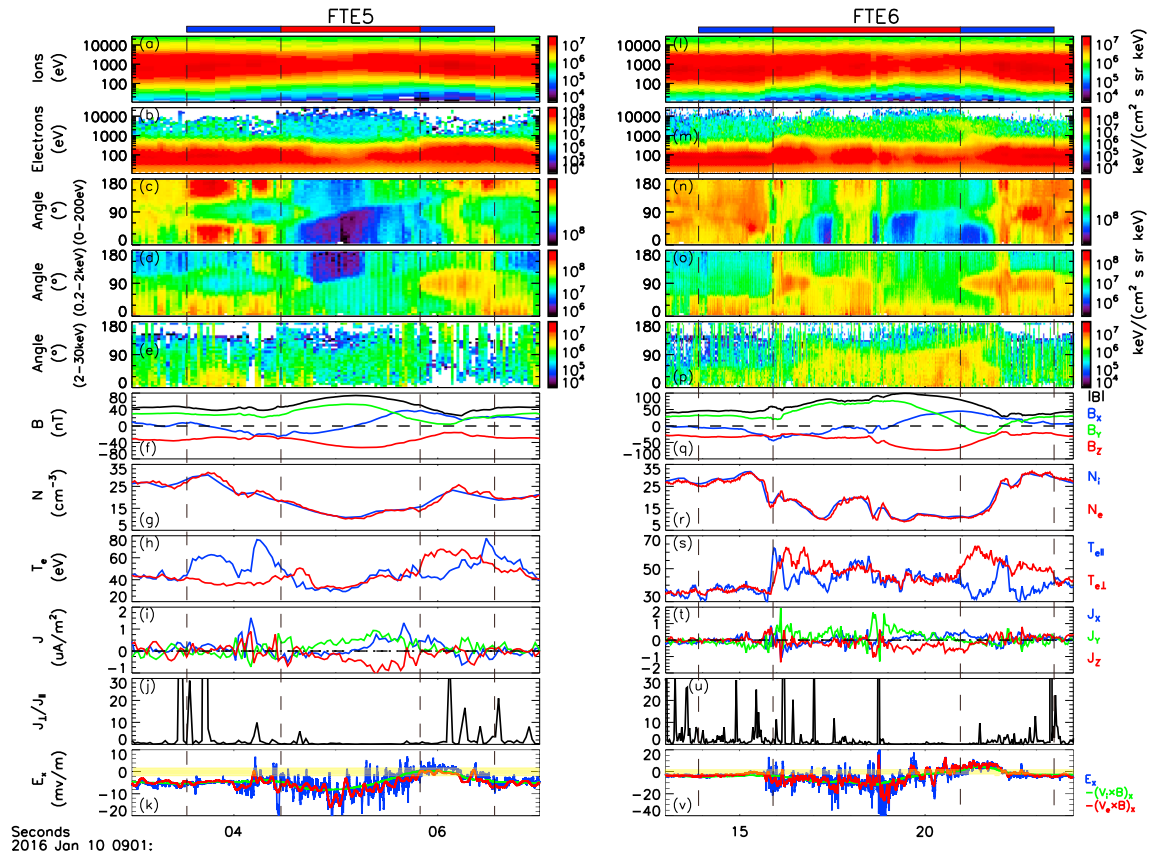


Figure 5. (a) Omnidirectional ion energy spectrum, (b) omnidirectional electron energy spectrum, (c) pitch angle spectrogram for 0 to 200 eV electrons, (d) pitch angle spectrogram for 0.2 to 2 keV electrons, (e) pitch angle spectrogram for 2 to 30 keV electrons, (f) three components and magnitude of magnetic field, (g) density, (h) electron temperature, (i) current density, (j) the ratio of J_{\perp}/J_{\parallel} , and (k) the electric field $E_x, -(\mathbf{V}_i \times \mathbf{B})_x, -(\mathbf{V}_e \times \mathbf{B})_x$, the shadow means the errors of E_x , for the FTE5. (l–v) The data in the same format for the FTE6.

These bidirectional low-energy electrons were generally interpreted as the entry of the magnetosheath electrons and subsequent reflection by the magnetic mirror (Hwang et al., 2016; Pu et al., 2013). Indeed, this kind of the electron distribution was commonly observed in the draping region where the magnetic field lines were reconnected recently between the magnetosheath and the magnetosphere. This can also explain why the bidirectional field-aligned distribution was observed in the core region of the FTE1, which was freshly created in the ion diffusion region. As the reconnection processed, this type of distribution in the earlier reconnected field lines would be changed due to less reflection and more electron precipitations and therefore disappeared in the core region of the mature FTEs. As a result, the low-energy magnetosheath electrons antiparallel to the magnetic field (toward the magnetosphere) and the medium and high-energy magnetosphere electrons parallel to the magnetic field (away from the magnetosphere) can be observed simultaneously in the core regions. The FTE6 had evolved for a long time since it was detected far away from the ion diffusion region. So the bidirectional field-aligned electron distributions in the draping regions were modified also.

In Figure 6, we plotted three typical electron distributions. Figures 6a, 6d, and 6g show electron velocity distribution functions cuts in $(V_B, V_B \times v)$ plane, where \mathbf{B} and \mathbf{v} are unit vectors of the magnetic field and the electron velocity, respectively. Figures 6b, 6e, and 6h show cuts perpendicular to \mathbf{B} . In the electron velocity distribution cuts containing the magnetic field direction V_B , electrons showed different distributions: bidirectional magnetosheath electrons along \mathbf{B} (Figure 6a), coexistence of the antiparallel-streaming magnetosheath electrons and parallel-streaming magnetosphere electrons (Figure 6d), and perpendicular-heated electrons (Figure 6g). In the plane perpendicular to the magnetic field, electrons displayed a highly gyrotropic distribution (Figures 6b, 6e, and 6h). Figures 6c, 6f, and 6i show electron fluxes as a function of energy, where the black, red, and blue lines represent cuts in the perpendicular, parallel, and antiparallel directions,

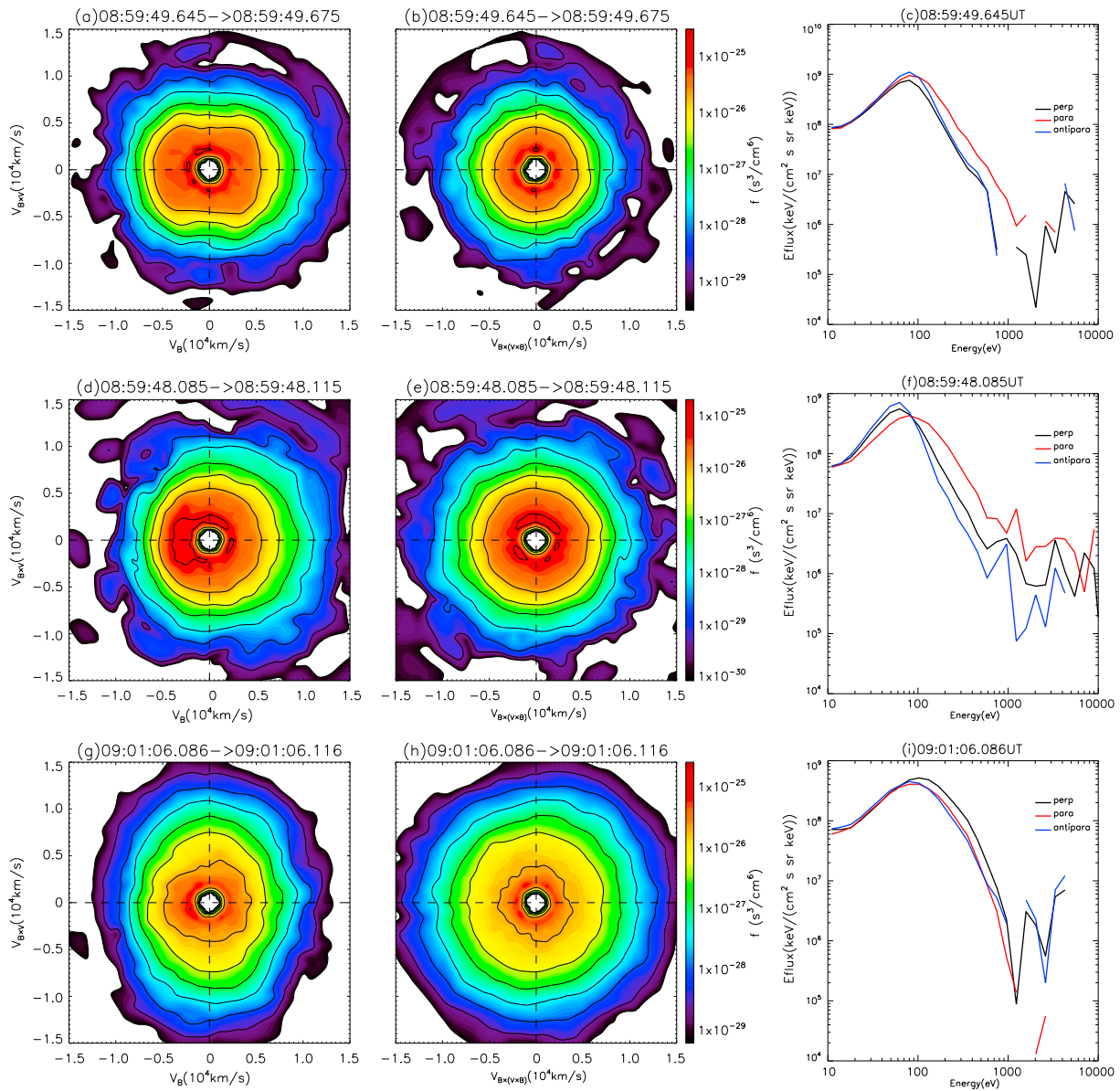


Figure 6. (a, d, and g) Electron velocity distribution functions cuts in plane (V_B , $V_B \times v$). (b, e, and h) Electron velocity distribution functions cuts in the plane perpendicular to B . (c, f, and i) Electron distributions at different pitch angles. The black, red, and blue lines represent cuts in the perpendicular, parallel, and antiparallel directions, respectively.

respectively. A bidirectional electron beam with the energy between 40 and 100 eV at 08:59:49.645 UT can be found in Figure 6c. In Figure 6f, an antiparallel electron beam with the energy between 20 and 80 eV can be seen at 08:59:48.085 UT. In Figure 6i, an enhancement of the perpendicular electron fluxes in the energy range of 80–800 eV can be seen.

The electron parallel temperature fell off remarkably in the core region of the FTEs (Figures 3h, 4h, 5h, and 5s) and was most weak inside the density dip, except for FTE1 where a sharp peak of $T_{e\parallel}$ was observed at the density dip. The electron perpendicular temperature did not show a remarkable variation in the FTEs 1–5. In the FTE6, the electron perpendicular temperature increased and was larger than the parallel temperature, especially in the trailing part of the draping regions of the FTE6 (Figure 5s).

The current density increased within each of the FTEs and had many fine structures in all three directions (Figures 3i, 4i, 5i, and 5t), consistent with the previous observation of the filamentary currents (Eastwood et al., 2016; Tang et al., 2018; Wang, Nakamura, et al., 2017). The ratio of $J_{\perp} / J_{\parallel}$ was very large in the

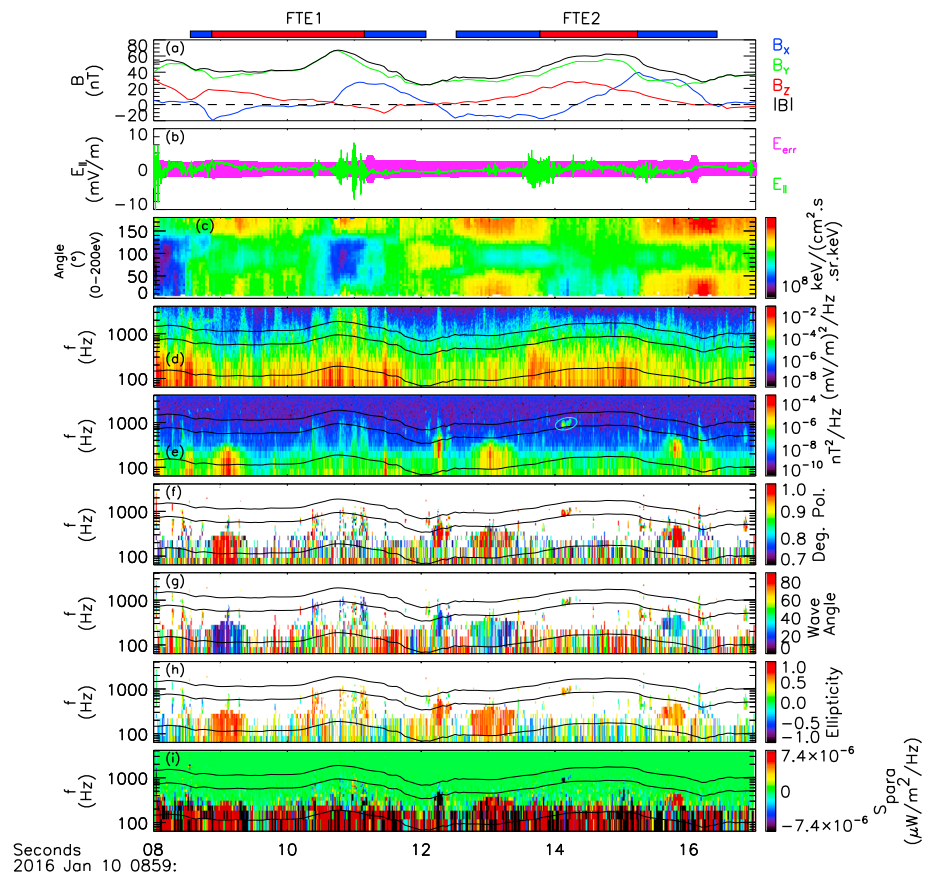


Figure 7. (a) Three components and magnitude of magnetic field, (b) parallel electric field, (c) pitch angle spectrogram for 0 to 200 eV electrons, (d, e) power spectral density of electric field and magnetic field, (f) degree of polarization, (g) wave angle, (h) ellipticity, and (i) parallel component of the Poynting vector for the FTE1 and FTE2. The black lines superposed on (d), (e), (f), (g), (h) and (i) correspond to 1, 0.5, and 0.1 the electron gyrofrequency.

draping regions of the FTEs and mostly close to 0 in the core regions of the FTEs (Figures 3j, 4j, 5j, and 5u). It indicates that the parallel current dominated in most of the core regions, and the perpendicular current was comparable to the parallel component or dominated in the draping regions of the FTEs, which is in agreement with the previous investigations of the magnetic flux ropes in the magnetotail and at the magnetopause (Wang, Nakamura, et al., 2017; Zhao et al., 2016).

Since the situation was almost the same in the three components of the electric field, only the x component of \mathbf{E} , $-(\mathbf{V}_i \times \mathbf{B})$, and $-(\mathbf{V}_e \times \mathbf{B})$ was present in Figures 3k, 4k, 5k, and 5v. There was an evident deviation between the E_x and $-(\mathbf{V}_i \times \mathbf{B})_x$ inside all of the FTEs, while E_x and $-(\mathbf{V}_e \times \mathbf{B})_x$ were in good agreement except for some localized regions with a sharp peak in E_x . Thus, the electrons were mainly frozen in the magnetic field and ions were not within these FTEs. In addition, the intense fluctuations of the electric field (e.g., E_x) were measured in each FTE and were mainly confined to the core region of the FTEs.

2.3. Waves Within FTEs

The electric field fluctuations were very strong inside the FTEs (Figures 7–10). These fluctuations are thought to be related to wave activities. The wave polarization analysis results are shown in Figures 7–10 for all of the FTEs in the same format. Figure 7 shows the result during the interval B including the FTE1 and FTE2. Figure 7a shows three components and magnitude of the magnetic field. The parallel electric field and low-energy electrons pitch angle distributions are displayed in Figures 7b and 7c. Figures 7d and 7e show the omnidirectional spectral power density of electric field and magnetic field. Figures 7f–7h show the results of the wave polarization analysis (Samson & Olson, 1980) using search-coil magnetometer waveforms, including the degree of polarization, wave angle, and ellipticity. Figure 7i shows the parallel

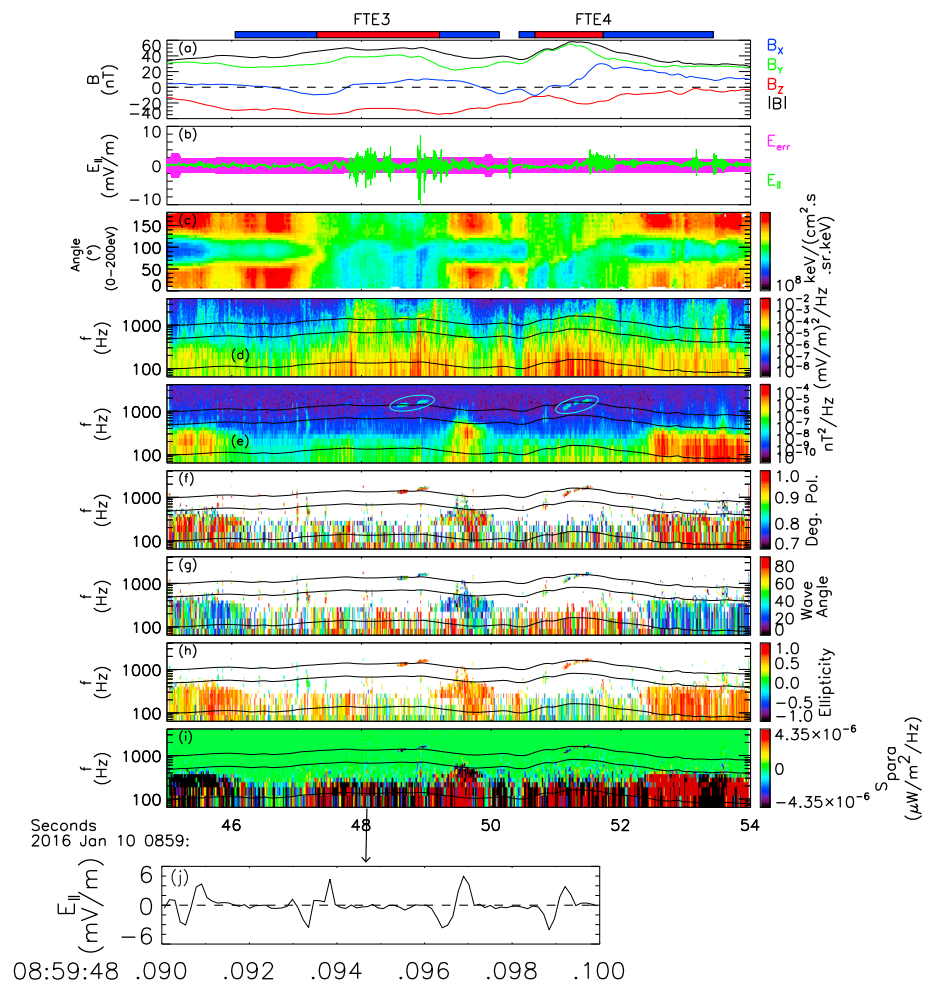


Figure 8. (a) Three components and magnitude of magnetic field, (b) parallel electric field, (c) pitch angle spectrogram for 0- to 200-eV electrons, (d, e) power spectral density of electric field and magnetic field, (f) degree of polarization, (g) wave angle, (h) ellipticity, (i) parallel component of the Poynting vector for the FTE3 and FTE4, and (j) parallel electric field. The black lines superposed on (d), (e), (f), (g), (h) and (i) correspond to 1, 0.5, and 0.1 the electron gyrofrequency.

component of the Poynting vector. The three curves in Figures 7d–7i to 10d–10i mean the frequencies of $0.1 f_{ce}$, $0.5 f_{ce}$, and $1.0 f_{ce}$, where f_{ce} is the electron gyrofrequency.

The strong broadband electrostatic emissions were observed inside all of the FTEs (Figures 7d, 8d, 9d, and 10d), consistent with the intense fluctuations from the waveform data shown in Figures 3k, 4k, 5k, and 5v. The strong parallel electric field was observed within all of the FTEs and mainly concentrated on the center region of the FTEs (Figures 7b, 8b, 9b, and 10b); its amplitude was, sometimes, up to 10 mV/m. A short period of the parallel electric field was enlarged in Figure 8j, and the bipolar signature of the parallel electric field represents the electrostatic solitary waves (Cattell, 2005; Deng et al., 2006; Khotyaintsev et al., 2010; Wang et al., 2013). The strong broadband emission was closely related to the amplification of the parallel electric field, which indicates that the broadband electrostatic emissions represent the electrostatic solitary waves, as pointed out previously by Matsumoto et al. (2003).

In addition to the electrostatic waves inside the FTEs, the strong electromagnetic emissions were found frequently around and within the FTEs (Figures 7–10). The enhancements of the electromagnetic emissions were observed in the frequency ranging from $\sim 0.1 f_{ce}$ to $\sim 0.5 f_{ce}$ in the draping regions of FTE1 and FTE2 (e.g., $\sim 08:59:09$, $\sim 08:59:12.3$, $\sim 08:59:13$, and $\sim 08:59:15.8$ UT in Figures 7d and 7e). The polarization analysis results suggest that the ellipticity was around 1.0 (Figure 7h), and the wave angle is less than 30° (Figure 7g) of these electromagnetic emissions. Thus, the electromagnetic emissions were the right-hand circular

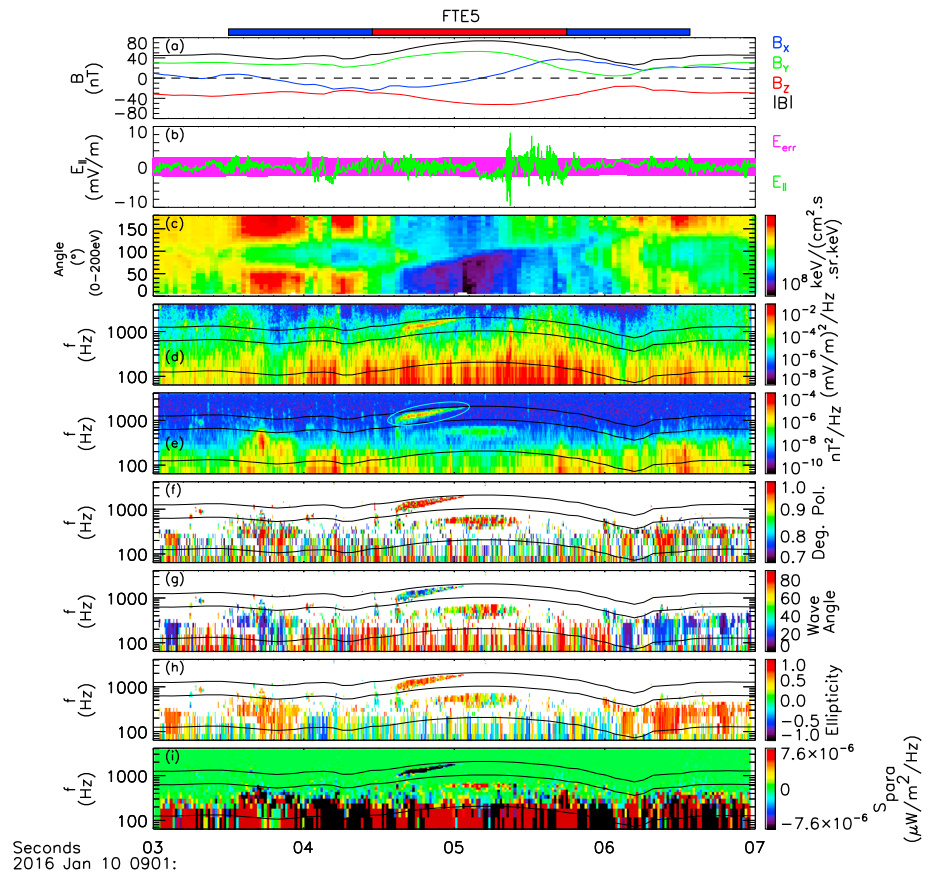


Figure 9. (a) Three components and magnitude of magnetic field, (b) parallel electric field, (c) pitch angle spectrogram for 0- to 200-eV electrons, (d, e) power spectral density of electric field and magnetic field, (f) degree of polarization, (g) wave angle, (h) ellipticity, and (i) parallel component of the Poynting vector for the FTE5. The black lines superposed on (d), (e), (f), (g), (h) and (i) correspond to 1, 0.5, and 0.1 the electron gyrofrequency.

polarization and they propagated quasi-parallel to the magnetic field, consistent with the whistler mode waves. The values of the Poynting vector were mainly positive at ~08:59:09, ~08:59:13, and ~08:59:15.8 UT, which indicates that the waves were propagating parallel to the magnetic field, whereas they were negative at ~08:59:12.3; that is, the waves were propagating antiparallel to the magnetic field. Given the magnetic field vectors at the locations with the whistler waves, B_y dominates for all three components and B_z was positive at ~08:59:09, ~08:59:13, and ~08:59:15.8 UT. It means that the waves in these areas were mainly propagating duskward and toward the expected X-line. For the waves at ~08:59:12.3, they were propagating downward. In the core region of the FTE2, another band of the whistler mode waves was observed at ~08:59:14.1 UT (marked with light blue ellipse), with a higher frequency above $0.5 f_{ce}$ and the wave normal angle of $\sim 60^\circ$ (Figure 7g). This oblique whistler mode wave was named as the upper band, while the whistler mode waves with the frequency between $\sim 0.1 f_{ce}$ and $\sim 0.5 f_{ce}$ were called the lower band in this paper.

The analogous upper band and lower band whistler mode waves were detected also around the other four FTEs. In the interval C (Figure 8), the lower band whistler waves were observed at ~08:59:45.5 UT (before FTE3), at ~08:59:49.6 UT (trailing part of the FTE3), and at ~08:59:53 UT (trailing part of the FTE4). The Poynting vector was antiparallel to the magnetic field at ~08:59:45.5 and ~08:59:49.6 UT. Namely, the lower band whistler waves were propagating toward the X-line at ~08:59:45.5 and ~08:59:49.6 UT. In contrast, the Poynting vector was both parallel and antiparallel during 08:59:52.5–08:59:54 UT; it indicates that the lower band waves were excited there.

The upper band whistler waves (marked with light blue ellipse in the Figure 8e) were observed very close to the centers of the FTE3 (at ~08:59:49 UT) and FTE4 (~08:59:51.5 UT). Their frequencies rose from $0.8 f_{ce}$ to

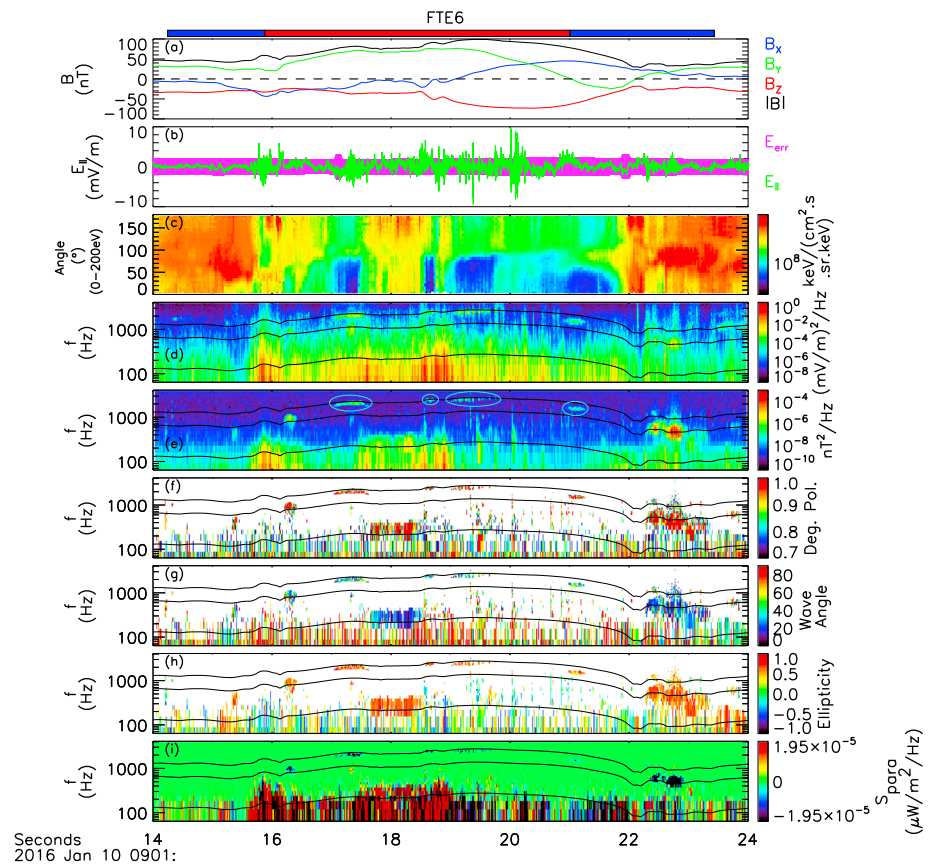


Figure 10. (a) Three components and magnitude of magnetic field, (b) parallel electric field, (c) pitch angle spectrogram for 0- to 200-eV electrons, (d, e) power spectral density of electric field and magnetic field, (f) degree of polarization, (g) wave angle, (h) ellipticity, and (i) parallel component of the Poynting vector for the FTE6. The black lines superposed on (d), (e), (f), (g), (h) and (i) correspond to 1, 0.5, and 0.1 the electron gyrofrequency.

$1.2 f_{ce}$ for FTE3 and from $0.7 f_{ce}$ to $1.1 f_{ce}$ for FTE4 (Figures 8d and 8e), the average wave angles were about 30° (Figure 8g), and the Poynting vectors were mainly antiparallel to the magnetic field (Figure 8i). Thus, the upper band whistler waves in the centers of the FTE3 and FTE4 were the rising tone whistler, as observed recently by Burch et al. (2018) at an electron diffusion region of the magnetopause reconnection but with the higher frequencies here.

At the FTE5 (Figure 9) and FTE6 (Figure 10), the lower band whistler waves were observed not only in the leading (at $\sim 09:01:03.7$ UT for FTE5 and $\sim 09:01:15.4$ UT for FTE6) and trailing (at $\sim 09:01:06.5$ UT for FTE5 and $\sim 09:01:22.8$ UT for FTE6) parts where the wave features were totally consistent with the observations in the draping regions of the FTEs 1–4 but also inside the FTE5 (at $\sim 09:01:05$ UT) and the FTE6 (at $09:01:18$ UT). Inside the FTE6, the lower band whistler waves were observed at $\sim 09:01:18$ UT and the wave characteristics were in agreement with the others. However, the lower band whistler waves inside the FTE5 presented some distinct features, especially the wave normal angle. For the lower band whistler waves in the FTE5, the frequency range was very narrow (from $0.25 f_{ce}$ to $0.35 f_{ce}$); contrary to the lower band whistler waves associated with other FTEs where the frequency range was broad, the normal angle was $\sim 80^\circ$ compared with the other lower band whistlers with the normal angle of $\sim 30^\circ$. Therefore, the lower band whistler waves inside the FTE5 were propagating near perpendicular to the magnetic field.

The upper band whistler waves were observed also inside the FTE5 and FTE6, analogous to the other FTEs 2–4. It was observed once at $09:01:04.7$ UT within FTE5 and multiple times (at $\sim 09:01:17.2$, $09:01:18.7$, $09:01:19.2$, and $09:01:21$ UT) inside FTE6. The upper band wave in the FTE5 was the typical rising tone, while that in the FTE6 kept nearly constant frequency of $1.0 f_{ce}$.

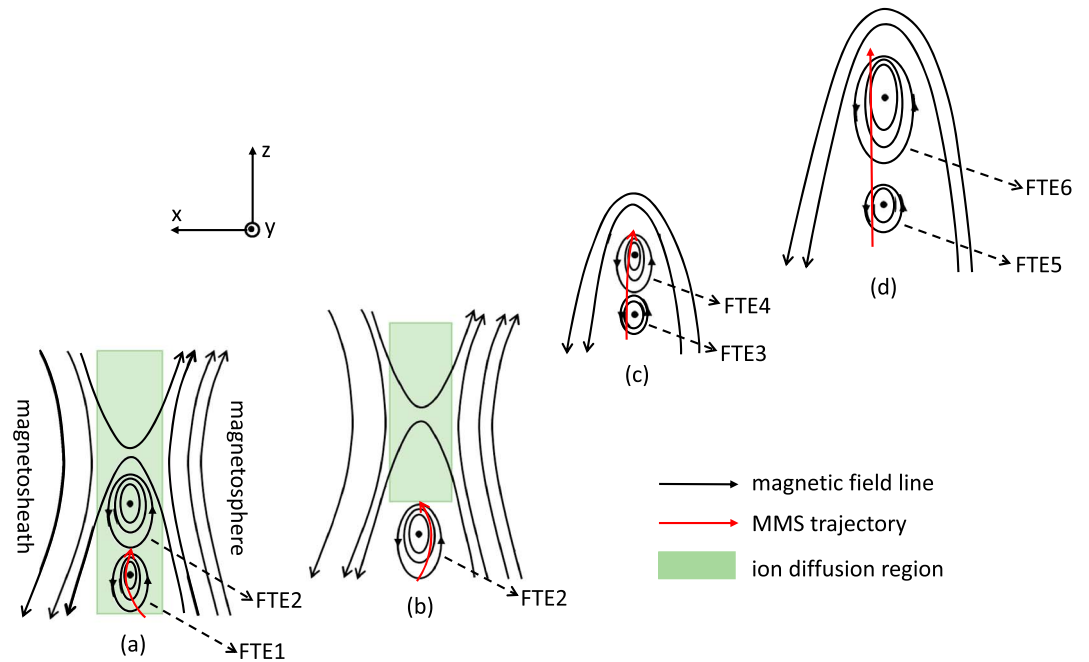


Figure 11. A sketch of the motion of the MMS relative to magnetopause, X-line, and all FTEs. MMS encounter with (a) FTE1, (b) FTE2, (c) FTEs 3 and 4, (d) FTEs 5 and 6. MMS = Magnetospheric Multiscale; FTE = flux transfer event.

Based on the analysis above, the whistler waves associated with the FTEs can be classified as the lower and upper bands. For the lower band whistler waves, they were observed always around the draping regions of the FTEs and sporadically in the core regions of the FTEs, propagated quasi-parallel/antiparallel to the magnetic field, and their frequencies were broad from $\sim 0.1 f_{ce}$ to $\sim 0.5 f_{ce}$, except for the one observed inside the FTE 5 where the lower band waves were propagating perpendicular to the magnetic field and the frequency was relatively narrow (between $0.25 f_{ce}$ and $0.35 f_{ce}$). We did not find any close correlation between the lower band whistler waves and the electron distribution. But in the trailing part of the draping region with the medium-energy electron flux enhancements, the lower band whistler waves were always observed.

For the upper band waves, they were only observed in the core regions of the FTEs and frequently near the FTEs center; their frequencies were very high ($\sim 1.0 f_{ce}$) and narrow, and they all propagated in the same direction (downward) as well as obliquely antiparallel to the magnetic field. The close correlation between the upper band waves and the dramatic depression of the low-energy electron fluxes along the 0° direction can be found during all of the upper band whistler waves. It appears that the upper band whistler waves

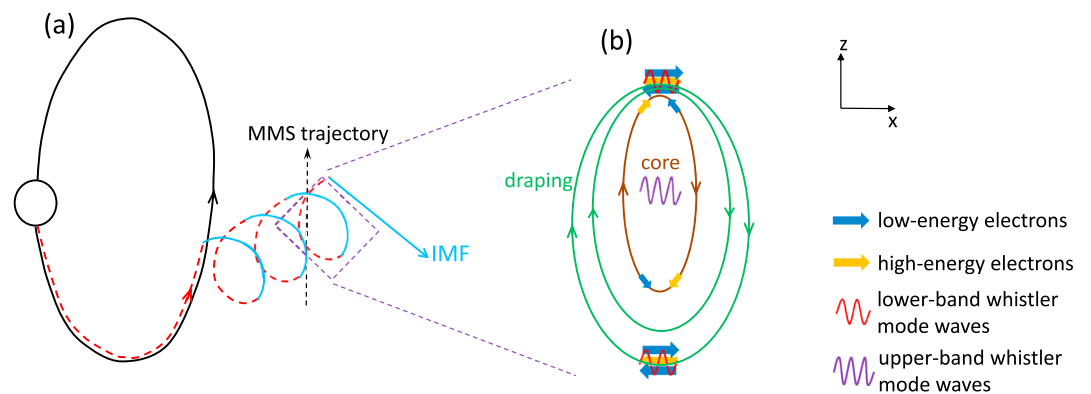


Figure 12. (a) A simplified sketch illustrating magnetic topology of the flux transfer event. (b) A sketch summarizing the observations of the electron pitch angle distributions in most flux transfer events. MMS = Magnetospheric Multiscale; IMF = interplanetary magnetic field.

came from the inner magnetosphere along the magnetic field lines and scattered the electrons along the 0° directions as they were propagating.

3. Discussion and Summary

In this paper, we report six FTEs observed at the magnetopause by the MMS mission. All of these six FTEs were embedded in the continuous southward ion flow, and the flow speeds were larger than 200 km/s. The sizes of the FTEs were estimated to be ion scale ($1.7\text{--}12.2d_i$). The first two FTEs were observed inside or next to a reconnection ion diffusion region, as illustrated in Figures 11a and 11b. After these two FTEs, although the southward ion flows were continuously observed, MMS has left the ion diffusion region. It means that the reconnection X-line was moving northward. About 30 s later, another two FTEs were encountered one by one, as shown in Figure 11c. Then, the FTEs 5 and 6 were observed about 1 min later (Figure 11d). During this entire interval, the southward ion flows were continuous. Thus, all of these FTEs should be generated in the process of the reconnection north of these FTEs. The FTEs 1–2 were located inside the ion diffusion region and thereby should be freshly created (Wang et al., 2010). While the other four FTEs were observed far away from the ion diffusion region and had left the source region. It should be noted that these six FTEs were observed before final magnetopause crossing from the magnetosheath side to the magnetosphere side at $\sim 09:20$ UT.

The electron pitch angle distributions around the FTEs were investigated in detail. The distributions greatly depended on the energy range and the corresponding subregions. The low-energy electrons mainly displayed the bidirectional field-aligned distribution: the fluxes near the 0° and 180° directions were significantly enhanced in the draping regions of the most FTEs except the FTE6. This type of the electron distribution could be caused by the reconnection of the field lines between the magnetosheath and the magnetosphere. Once the reconnection occurred at the magnetopause, the magnetosheath low-energy electrons immediately entered into the magnetosphere and then were reflected, which led to the bidirectional field-aligned distribution of the magnetosheath electrons. As the reconnection extended in the normal direction of the magnetopause, the earlier reconnected field lines moved into the core region and bidirectional field-aligned electron distribution disappeared because there are more electron precipitations into the auroral region. Consequently, the low-energy electrons antiparallel to the magnetic field (toward the magnetosphere) and the medium-/high-energy electrons parallel to the magnetic field (away from the magnetosphere) were observed at the same time in the core regions. A simplified sketch is shown in Figure 12 to illustrate this observed electron distributions (Figure 12b) and possible magnetic topology of the FTE (Figure 12a).

While the FTEs were moving southward and away from the reconnection diffusion regions, the magnetic field component B_x was easily compressed in the tailing part of the FTEs due to the electron convection motion, and thereby, a pileup region was generated there, as shown in Figures 3f, 4f, 5f, and 5q. Then, the electrons can be accelerated in the pileup region via the betatron acceleration (Fu et al., 2011; Huang et al., 2015). Therefore, the enhancements of the medium-energy electrons near 90° directions could be observed in the trailing part of the draping region. This electron acceleration resulted in the electron temperature anisotropy for medium energies (e.g., between 80 and 800 eV in Figure 6i). Then, the lower band whistlers were excited locally due to this electron temperature anisotropy.

A variety of wave modes have been reported in the flux ropes at the magnetopause and in the magnetotail, for example, electron holes (Khotyaintsev et al., 2010), lower hybrid frequency range waves (Wang et al., 2016; Zhou et al., 2009), and whistler mode waves (Huang et al., 2016; Kennel et al., 1986). Graham et al. (2016) reported that the electrostatic solitary waves observed at the magnetopause can be generated by the beam plasma instability, the warm bistreaming instability, and electron-ion instabilities. In our study, the electrostatic solitary waves are observed in the core region of FTEs, where counterstreaming magnetosheath and magnetosphere electrons dominate. So the beam plasma instability (e.g., an antiparallel electron beam with the energy between 20 and 80 eV in Figure 6f) can be one potential candidate for the generation of the electrostatic solitary waves.

The whistler mode waves were frequently observed around the FTEs and classified as the lower and higher bands. As for the lower band whistler waves, the frequency range was relatively broad from $\sim 0.1 f_{ce}$ to $\sim 0.5 f_{ce}$, the normal angle was generally less than 30° , and the Poynting vector was negative or positive or both in

one event. Moreover, the lower band waves were observed in the ion diffusion region as well (not shown). It indicates that the lower band whistler waves were excited locally and then propagated toward or away from the X-line. The compressed tailing part of the FTEs was one source region of the lower band whistler waves, since the electron anisotropy produced by betatron acceleration in the perpendicular direction can be formed in that region.

All of the upper band whistler waves were observed in the core regions of these FTEs. The wave characteristics were uniform, for example, the frequency range was very narrow ($\sim 1.0 f_{ce}$), the normal angle is about 50° , that is, very oblique waves, and most of the upper band waves showed a rising tone feature. Thus, it seems that these upper band waves originated from the same source region. As they propagated in the core region, they scattered the low-energy electrons parallel to the magnetic field and caused the depression of the low-energy electron fluxes in these directions. Our observation indicates that the whistler mode waves have many sources at the magnetopause, not only directly generated by the reconnection at the electron diffusion region as suggested previously (Burch et al., 2018; Cao et al., 2017; Deng & Matsumoto, 2001). They can be generated in the draping regions of the FTEs, especially the tailing part.

In summary, a series of six ion-scale FTEs at the magnetopause were observed in the southward reconnection outflows. The first two FTEs were adjacent to the ion diffusion region while the other four FTEs were found away from the ion diffusion region. The electron distribution was distinct in the different regions of the FTEs. In the draping region, the low-energy electrons generally displayed the bidirectional field-aligned distribution except for the last one, which had evolved for a long time after generation. The medium-energy electrons showed the pancake distribution in the trailing part of the draping regions while exhibited the bidirectional or the beam distribution in the leading part of the draping regions. The whistler waves were frequently observed around and within the FTEs and classified as the lower band and upper band based on the frequency range. The lower band waves were broad, quasi-parallel/antiparallel propagation; the frequencies were less than half of the electron gyrofrequency and could be excited locally. The upper band waves were narrow and oblique, only observed in the core regions, and could originate from the same region. The upper band whistler waves effectively scattered the low-energy electrons along the magnetic field.

Acknowledgments

All the MMS data used in this work are available at the MMS data center (<https://lasp.colorado.edu/mms/sdc/>). This work is supported by the National Science Foundation of China (NSFC) grants (41674143, 41474126, 41331067, and 41421063) and by the National Basic Research Program of China (2013CBA01503).

References

- Burch, J. L., Moore, T. E., Torbert, R. B., & Giles, B. L. (2016). Magnetospheric Multiscale overview and science objectives. *Space Science Reviews*, *199*, 5–21. <https://doi.org/10.1007/s11214-015-0164-9>
- Burch, J. L., Webster, J. M., Genestreti, K. J., Torbert, R. B., Giles, B. L., Fuselier, S. A., et al. (2018). Wave phenomena and beam-plasma interactions at the magnetopause reconnection region. *Journal of Geophysical Research: Space Physics*, *123*, 1118–1133. <https://doi.org/10.1002/2017JA024789>
- Cao, D., Fu, H. S., Cao, J. B., Wang, T. Y., Graham, D. B., Chen, Z. Z., et al. (2017). MMS observations of whistler waves in electron diffusion region. *Geophysical Research Letters*, *44*, 3954–3962. <https://doi.org/10.1002/2017GL072703>
- Cattell, C. (2005). Cluster observations of electron holes in association with magnetotail reconnection and comparison to simulations. *Journal of Geophysical Research*, *110*, A01211. <https://doi.org/10.1029/2004JA010519>
- Deng, X. H., & Matsumoto, H. (2001). Rapid magnetic reconnection in the Earth's magnetosphere mediated by whistler waves. *Nature*, *410*(6828), 557–560. <https://doi.org/10.1038/35069018>
- Deng, X. H., Tang, R. X., Matsumoto, H., Pickett, J. S., Fazakerley, A. N., Kojima, H., et al. (2006). Observations of electrostatic solitary waves associated with reconnection by Geotail and Cluster. *Reconnection at Sun and in Magnetospheres*, *37*(7), 1373–1381. <https://doi.org/10.1016/j.asr.2005.05.129>
- Eastwood, J. P., Phan, T. D., Cassak, P. A., Gershman, D. J., Haggerty, C., Malakit, K., et al. (2016). Ion-scale secondary flux ropes generated by magnetopause reconnection as resolved by MMS. *Geophysical Research Letters*, *43*, 4716–4724. <https://doi.org/10.1002/2016GL068747>
- Ergun, R. E., Tucker, S., Westfall, J., Goodrich, K. A., Malaspina, D. M., Summers, D., et al. (2016). The axial double probe and fields signal processing for the MMS mission. *Space Science Reviews*, *199*, 167–188. <https://doi.org/10.1007/s11214-014-0115-x>
- Fear, R. C., Milan, S. E., Fazakerley, A. N., Lucek, E. A., Cowley, S. W. H., & Dandouras, I. (2008). The azimuthal extent of three flux transfer events. *Annales de Geophysique*, *26*(8), 2353–2369. <https://doi.org/10.5194/angeo-26-2353-2008>
- Fu, H. S., Khotyaintsev, Y. V., Andre, M., & Vaivads, A. (2011). Fermi and betatron acceleration of suprathermal electrons behind dipolarization fronts. *Geophysical Research Letters*, *38*, L16104. <https://doi.org/10.1029/2011GL048528>
- Graham, D. B., Khotyaintsev, Y. V., Vaivads, A., & Andre, M. (2016). Electrostatic solitary waves and electrostatic waves at the magnetopause. *Journal of Geophysical Research: Space Physics*, *121*, 3069–3092. <https://doi.org/10.1002/2015JA021527>
- Hasegawa, H., Wang, J., Dunlop, M. W., Pu, Z. Y., Zhang, Q. H., Lavraud, B., et al. (2010). Evidence for a flux transfer event generated by multiple X-line reconnection at the magnetopause. *Geophysical Research Letters*, *37*, L16101. <https://doi.org/10.1029/2010GL044219>
- Huang, C., Wu, M. Y., Lu, Q. M., Wang, R. S., & Wang, S. (2015). Electron acceleration in the dipolarization front driven by magnetic reconnection. *Journal of Geophysical Research: Space Physics*, *120*, 1759–1765. <https://doi.org/10.1002/2014JA020918>
- Huang, S. Y., Sahrour, F., Retino, A., le Contel, O., Yuan, Z. G., Chasapis, A., et al. (2016). MMS observations of ion-scale magnetic island in the magnetosheath turbulent plasma. *Geophysical Research Letters*, *43*, 7850–7858. <https://doi.org/10.1002/2016GL070033>

- Hwang, K. J., Sibeck, D. G., Giles, B. L., Pollock, C. J., Gershman, D., Avakov, L., et al. (2016). The substructure of a flux transfer event observed by the MMS spacecraft. *Geophysical Research Letters*, *43*, 9434–9443. <https://doi.org/10.1002/2016GL070934>
- Kawano, H., & Russell, C. T. (1997). Survey of flux transfer events observed with the ISEE 1 spacecraft: Dependence on the interplanetary magnetic field. *Journal of Geophysical Research*, *102*(A6), 11,307–11,313. <https://doi.org/10.1029/97JA00481>
- Kennel, C. F., Coroniti, F. V., & Scarf, F. L. (1986). Plasma waves in magnetotail flux ropes. *Journal of Geophysical Research*, *91*(A2), 1424–1438. <https://doi.org/10.1029/JA091iA02p01424>
- Khotyaintsev, Y. V., Vaivads, A., Andre, M., Fujimoto, M., Retino, A., & Owen, C. J. (2010). Observations of slow electron holes at a magnetic reconnection site. *Physical Review Letters*, *105*, 165002. <https://doi.org/10.1103/PhysRevLett.105.165002>
- Le Contel, O., et al. (2016). The search-coil magnetometer for MMS. *Space Science Reviews*, *199*(1–4), 257–282.
- Lee, L. C., & Fu, Z. F. (1985). A theory of magnetic-flux transfer at the Earth's magnetopause. *Geophysical Research Letters*, *12*(2), 105–108. <https://doi.org/10.1029/GL012i002p00105>
- Lindqvist, P. A., Olsson, G., Torbert, R. B., King, B., Granoff, M., Rau, D., et al. (2016). The spin-plane double probe electric field instrument for MMS. *Space Science Reviews*, *199*(1–4), 137–165. <https://doi.org/10.1007/s11214-014-0116-9>
- Matsumoto, H., Deng, X. H., Kojima, H., & Anderson, R. R. (2003). Observation of electrostatic solitary waves associated with reconnection on the dayside magnetopause boundary. *Geophysical Research Letters*, *30*(6), 1326. <https://doi.org/10.1029/2002GL016319>
- Oieroset, M., et al. (2011). Direct evidence for a three-dimensional magnetic flux rope flanked by two active magnetic reconnection X lines at Earth's magnetopause. *Physical Review Letters*, *107*(16), 165007. <https://doi.org/10.1103/PhysRevLett.107.165007>
- Owen, C. J., Marchaudon, A., Dunlop, M. W., Fazakerley, A. N., Bosqued, J. M., Dewhurst, J. P., et al. (2008). Cluster observations of “crater” flux transfer events at the dayside high-latitude magnetopause. *Journal of Geophysical Research*, *113*, A07S04. <https://doi.org/10.1029/2007JA012701>
- Paschmann, G., Haerendel, G., Papamastorakis, I., Sckopke, N., Bame, S. J., Gosling, J. T., & Russell, C. T. (1982). Plasma and magnetic field characteristics of magnetic flux transfer events. *Journal of Geophysical Research*, *87*(A4), 2159–2168. <https://doi.org/10.1029/JA087iA04p02159>
- Pollock, C., Moore, T., Jacques, A., Burch, J., Gliese, U., Saito, Y., et al. (2016). Fast plasma investigation for Magnetospheric Multiscale. *Space Science Reviews*, *199*(1–4), 331–406. <https://doi.org/10.1007/s11214-016-0245-4>
- Pu, Z. Y., Raeder, J., Zhong, J., Bogdanova, Y. V., Dunlop, M., Xiao, C. J., et al. (2013). Magnetic topologies of an in vivo FTE observed by Double Star/TC-1 at Earth's magnetopause. *Geophysical Research Letters*, *40*, 3502–3506. <https://doi.org/10.1002/grl.50714>
- Russell, C. T., Anderson, B. J., Baumjohann, W., Bromund, K. R., Dearborn, D., Fischer, D., et al. (2016). The Magnetospheric Multiscale magnetometers. *Space Science Reviews*, *199*(1–4), 189–256. <https://doi.org/10.1007/s11214-014-0057-3>
- Russell, C. T., & Elphic, R. C. (1978). Initial ISEE magnetometer results—Magnetopause observations. *Space Science Reviews*, *22*(6), 681–715.
- Samson, J. C., & Olson, J. V. (1980). Some comments on the descriptions of the polarization states of waves. *Geophysical Journal of the Royal Astronomical Society*, *61*(1), 115–129. <https://doi.org/10.1111/j.1365-246X.1980.tb04308.x>
- Saunders, M. A., Russell, C. T., & Sckopke, N. (1984). Flux transfer events: Scale size and interior structure. *Geophysical Research Letters*, *11*(2), 131–134. <https://doi.org/10.1029/GL011i002p00131>
- Scholer, M. (1988). Magnetic-flux transfer at the magnetopause based on single X-line bursty reconnection. *Geophysical Research Letters*, *15*(4), 291–294. <https://doi.org/10.1029/GL015i004p00291>
- Schwartz, S. J. (1998). Shock and discontinuity normals, mach numbers and related parameters. In G. Paschmann, & P. W. Daly (Eds.), *Analysis methods for multi-spacecraft data*, (pp. 249–270). Bern: International Space Science Institute.
- Shi, Q. Q., Shen, C., Dunlop, M. W., Pu, Z. Y., Zong, Q. G., Liu, Z. X., et al. (2006). Motion of observed structures calculated from multipoint magnetic field measurements: Application to Cluster. *Geophysical Research Letters*, *33*, L08109. <https://doi.org/10.1029/2005GL025073>
- Shi, Q. Q., Shen, C., Pu, Z. Y., Dunlop, M. W., Zong, Q. G., Zhang, H., et al. (2005). Dimensional analysis of observed structures using multipoint magnetic field measurements: Application to Cluster. *Geophysical Research Letters*, *32*, L12105. <https://doi.org/10.1029/2005GL022454>
- Shi, Q. Q., Zong, Q. G., Fu, S. Y., Dunlop, M. W., Pu, Z. Y., Parks, G. K., et al. (2013). Solar wind entry into the high-latitude terrestrial magnetosphere during geomagnetically quiet times. *Nature Communications*, *4*(1), 1466. <https://doi.org/10.1038/ncomms2476>
- Southwood, D. J., Farrugia, C. J., & Saunders, M. A. (1988). What are flux-transfer events. *Planetary and Space Science*, *36*(5), 503–508. [https://doi.org/10.1016/0032-0633\(88\)90109-2](https://doi.org/10.1016/0032-0633(88)90109-2)
- Tan, B., Lin, Y., Perez, J. D., & Wang, X. Y. (2011). Global-scale hybrid simulation of dayside magnetic reconnection under southward IMF: Structure and evolution of reconnection. *Journal of Geophysical Research*, *116*, A02206. <https://doi.org/10.1029/2010JA015580>
- Tang, B. B., et al. (2018). Magnetic depression and electron transport in an ion-scale flux rope associated with Kelvin-Helmholtz waves. *Annales de Geophysique*, *36*(3), 879–889. <https://doi.org/10.5194/angeo-36-879-2018>
- Teh, W. L., Denton, R. E., Sonnerup, B. U. O., & Pollock, C. (2017). MMS observations of oblique small-scale magnetopause flux ropes near the ion diffusion region during weak guide-field reconnection. *Geophysical Research Letters*, *44*, 6517–6524. <https://doi.org/10.1002/2017GL074291>
- Teh, W.-L., Nakamura, T. K. M., Nakamura, R., Baumjohann, W., Russell, C. T., Pollock, C., et al. (2017). Evolution of a typical ion-scale magnetic flux rope caused by thermal pressure enhancement. *Journal of Geophysical Research: Space Physics*, *122*, 2040–2050. <https://doi.org/10.1002/2016ja023777>
- Varsani, A., Owen, C. J., Fazakerley, A. N., Forsyth, C., Walsh, A. P., Andre, M., et al. (2014). Cluster observations of the substructure of a flux transfer event: Analysis of high-time-resolution particle data. *Annales de Geophysique*, *32*(9), 1093–1117. <https://doi.org/10.5194/angeo-32-1093-2014>
- Wang, R., Du, A., Nakamura, R., Lu, Q., Khotyaintsev, Y. V., Volwerk, M., et al. (2013). Observation of multiple sub-cavities adjacent to single separatrix. *Geophysical Research Letters*, *40*, 2511–2517. <https://doi.org/10.1002/grl.50537>
- Wang, R., Lu, Q., Nakamura, R., Baumjohann, W., Russell, C. T., Burch, J. L., et al. (2017). Interaction of magnetic flux ropes via magnetic reconnection observed at the magnetopause. *Journal of Geophysical Research: Space Physics*, *122*, 10,436–10,447. <https://doi.org/10.1002/2017JA024482>
- Wang, R., Nakamura, R., Lu, Q., Baumjohann, W., Ergun, R. E., Burch, J. L., et al. (2017). Electron-scale quadrants of the Hall magnetic field observed by the Magnetospheric Multiscale spacecraft during asymmetric reconnection. *Physical Review Letters*, *118*, 175101. <https://doi.org/10.1103/PhysRevLett.118.175101>

- Wang, R. S., Lu, Q. M., Du, A. M., & Wang, S. (2010). In situ observations of a secondary magnetic island in an ion diffusion region and associated energetic electrons. *Physical Review Letters*, *104*(17), 175,003. <https://doi.org/10.1103/PhysRevLett.104.175003>
- Wang, R. S., Lu, Q. M., Nakamura, R., Huang, C., Li, X., Wu, M. Y., et al. (2016). Electrostatic and electromagnetic fluctuations detected inside magnetic flux ropes during magnetic reconnection. *Journal of Geophysical Research: Space Physics*, *121*, 9473–9482. <https://doi.org/10.1002/2016JA022906>
- Yao, S. T., Shi, Q. Q., Li, Z. Y., Wang, X. G., Tian, A. M., Sun, W. J., et al. (2016). Propagation of small size magnetic holes in the magnetospheric plasma sheet. *Journal of Geophysical Research: Space Physics*, *121*, 5510–5519. <https://doi.org/10.1002/2016JA022741>
- Zhang, H., Kivelson, M. G., Angelopoulos, V., Khurana, K. K., Pu, Z. Y., Walker, R. J., et al. (2012). Generation and properties of in vivo flux transfer events. *Journal of Geophysical Research*, *117*, A05224. <https://doi.org/10.1029/2011JA017166>
- Zhao, Y., Wang, R. S., & Du, A. M. (2016). Characteristics of field-aligned currents associated with magnetic flux ropes in the magnetotail: A statistical study. *Journal of Geophysical Research: Space Physics*, *121*, 3264–3277. <https://doi.org/10.1002/2015JA022144>
- Zhou, M., Deng, X. H., Li, S. Y., Pang, Y., Vaivads, A., Rème, H., et al. (2009). Observation of waves near lower hybrid frequency in the reconnection region with thin current sheet. *Journal of Geophysical Research*, *114*, A02216. <https://doi.org/10.1029/2008JA013427>